Airflow Measurement Across Negatively Infiltration Processed Porous Aluminum Structures

A. J. Otaru and H. P. Morvan
Gas Turbine and Transmissions Research Centre, Faculty of Engineering, The University of Nottingham, Nottingham, NG7 2RD, U.K.

A. R. Kennedy
Engineering Dept., Lancaster University, Lancaster, LA1 4YW, U.K.

DOI 10.1002/aic.16523
Published online January 17, 2019 in Wiley Online Library (wileyonlinelibrary.com)

Detailed structural characterization and experimental measurement of airflow across open-celled aluminum foam structures with near-spherical cells varying in pore sizes and interstices are presented herein. The aluminum foam structures were produced by infiltrating liquid aluminum into convergent gaps created by packed beds of near-spherical hydrosoft salt beds varying in particle sizes, packing densities, and infiltration pressures. A quantitative assessment of the unit pressure drops developed across these structures show that viscous and inertial terms of these structures were observed to greatly depend on the shape and structural macroscopic parameters of the porous medium. © 2019 American Institute of Chemical Engineers *AIChE J*, 65: 1355–1364, 2019
Keywords: porous metal, measurement, pore sizes, openings

Introduction

Engineers and scientists in the past have determined the permeabilities of many soils and sands varying in degree of particle sizes and interstices measured in Darcy (D) or milliDarcy (mD) to avoid the intricacy of prefixes like terms (10^{-09}, 10^{-10}, 10^{-11}, 10^{-12}, etc.). The numerical value of permeability, k_0, measured in the horizontal or vertical plane for a given packed beds of rocks depends on the degree of its particle sizes and interstices[1] and the addition of a correction factor, Kozeny constant,[2-6] was proposed to bridge the gap between analytical model and reality due to the anisotropic and complicated tortuous flow paths of the porous medium.

While the packed beds are often made from packing of naturally occurring rocks and sands, artificially made porous structures made from metals and alloys such as metal foam (aluminum, nickel, titanium, copper, steel, etc.) are remarkably useful as structures that interact with a fluid in processes like sound absorption, filtration and catalysis, heat exchange and storage, and so forth. An important feature of this structure is the resistance provided by its skeletal configuration when presented to flowing fluid across the pores and interstices of the porous matrix, often described by the unit pressure drop developed across the inlet and exit of the structure as a function of superficial fluid velocity and properties of the fluid. Measuring or estimating and controlling the unit pressure drop developed across this structure is imperative to the design of porous metallic structures with enhanced performance.

Correspondence concerning this article should be addressed to A. J. Otaru at otaru_12257@yahoo.com

Flow through open-celled metallic foams (Figure 1) are more complicated by the opening of its windows or interconnection of its pores.[8] This interconnection in porous metal foam enabled its high porosity, permeability, large foam surface area per unit bulk volume (specific surface) and thermal conductivity[9-11] which has made it beneficial for use as pressure reduction and heat transfer devices.[11] Understanding the behavior of fluid flow through commercially available porous metallic structures like Porvair, Recemat, Alantum, Alporas, Duocel, and so forth with open porosities between 80 and 95% has been proven experimentally in Ref.12-15. The unidirectional (horizontal) flow permeability and inertial coefficient were calculated by fitting the pressure and velocity data into the so called two-term Hazen–Dupuit–Darcy also known as Darcy–Forchheimer (D-F) model (Eq. 1). This two term D-F equation relates the developed pressure gradient (∇P) for a moving fluid across porous medium as a function of velocity vector (v_s), permeability (k_o), fluid density (ρ), fluid dynamic viscosity (μ), and the Forchheimer coefficient (C_F).

$$-\frac{\partial p}{\partial x_i} = \nabla p = \frac{\mu}{k_o} v_s + \rho \frac{C_F}{\sqrt{k_o}} v_s^2 \tag{1}$$

Generally, the pressure drop per unit thickness (∇P) of any porous structure in the Phillipe Forchheimer model can be expressed solitarily in the first term of the LHS of the Eq. 1 only at very low velocities (Darcy regime) where losses are mainly due to skin friction while the second term predominates at high velocities (laminar-turbulent regime) where viscous forces are negligible while contraction and enlargement are significant[16,17] (see Eq. 2). In addition, extremely high Reynolds number fluid flow could result in the continuous

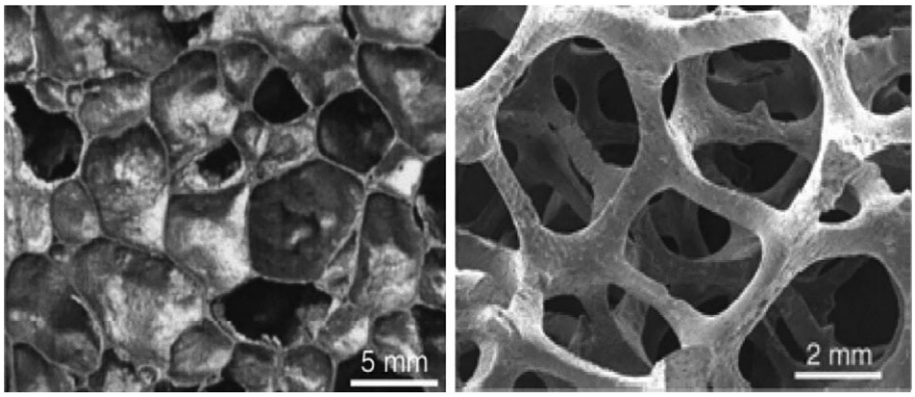

Figure 1. Images of close (left) and open (right) celled metallic foam structures.

Adapted from Ref. 7.

addition of non-Darcy pressure drop and increased drag or inertial forces and the relationship between the pressure drop gradient and superficial fluid velocity, in some porous structures, can be corrected[18] by the power law or three-term cubic Forchheimer models as shown by Eqs. 3 and 4, respectively.

$$\nabla p = A v_s \tag{2}$$

$$-\frac{\partial p}{\partial x_i} = \nabla p = A v_s + B v_s^m \; (1.6 \le m \le 2.0) \tag{3}$$

$$-\frac{\partial p}{\partial x_i} = \nabla p = A v_s + B v_s^2 + C v_s^3 \tag{4}$$

where A and B are related to the viscous inertial terms and fluid properties in Eq. 1 while the last term, *C*, in the three-term cubic Forchheimer (Eq. 4) model was introduced[18] to make the equation reasonably fit to experimental results.

Realistically, the infiltration of liquid metal into near-spherical beds of sacrificial porogens or space fillers has been proven[19,20] to produce low-density porous "bottleneck-type" materials. Computational fluid dynamics (CFD) simulation[21] and flow measurement[22] across the low-density porous structure of similar pore sizes and different openings point the permeability of this structure to greatly depend on the sizes of the openings connecting the spherical pores. In this work, a full description of the measurement and flow behavior of porous aluminum structures having different pore sizes and pore diameter openings is studied to see what benefit therein.

Structural Characterization and Airflow Measurement

Similar experimental procedure on the production of aluminum (Al) foam structure (University of Nottingham, UK) made by replication-casting process[19,20,22] was used to produce foam structures used in this work by negatively infiltrating liquid melts into packed beds of near-spherical hydrosoft-based (sodium chloride) salts. In brief, near-spherical salts of the different sizes typically in the ranges X/1.0–1.4 mm, Y/2.0–2.5 mm, and Z/2.5–3.15 mm (Figure 2) were packed in a 40 mm diameter and 50 mm height vessel and liquid aluminum were driven into the interstices of the beds at some applied differential pressures typically between 0.25 and 0.90 bar. Preheating of the space fillers to within 450–600 °C was done prior to packing to avoid premature solidification of the melt. The pore volume fractions of the porous structures were measured based on their mass-scale difference using digital scales and Vernier caliper while optical images of the structures assessed in Image J software reveal in detail, the pore diameter sizes, and openings. Scanning electron microscope (SEM) of the salt samples and optical images of the foam structures produces are presented in Figure 2.

Advanced imaging techniques working from x-ray computerized tomography (CT) data were also used to enable assessment of the structural properties (pore sizes, openings, roundness, and volume) of the porous materials at microscale level as shown in Figure 3. In brief, high resolution (26 μm voxel dimension in x, y, and z) two-dimensional stack images (Figure 3a) were restored to three-dimensional (3-D) volume (Figure 3b) in ScanIP module of Simpleware™ (advanced 3D imaging, meshing and physics solving software currently owned by Synopsys computer integrated systems design company). Image processing procedure like thresholding, segmentation, filtering, and various image editing tools available within the ScanIP were used to create the 3-D volume and to also ensure the right structural material is preserved. A workable representative volume (Figure 3c) was obtained by shrinking large volume of image data until porosity differed by ±2% and the fluid phase (Figure 3d) of the representative matrix was obtained by inverting the masked structural phase. A watershed segmentation was carried out on the fluid domain matrix by disconnecting the particles to enable evaluation of the mean particle/pore sizes of the porous matrix in ScanIP. Additionally, pore diameter openings of the structures were measured by running a centreline across the representative matrix and a mean value of the smaller diameter (openings) was taken and compared to measuring these openings directly in ScanIP as evident by Figure 3g and that obtained using SEM and optical micrograph techniques.

Table 1 presents the macroscopic and flow (to be discussed later) parameters for the different porous metallic structures produced using hydrosoft-based salts for particle sizes in the range of 1.0–1.4 mm, 2.0–2.5 mm, and 2.5–3.15 mm represented by the following symbols (X, Y, and Z) in the table. X1 (1.0–1.4 mm) and Z1 (2.5–3.15 mm) structures were produced using a liquid metal infiltration pressure of 0.9 bar while the Y (2.0–2.5 mm) structures were produced at 0.90 (Y1), 0.50 (Y2), 0.33 (Y3), and 0.25 (Y4) bars. Key parameters like porosity, mean pore size, and mean openings or connectivity measured are presented in Table 1. As expected, structural measurements of pore sizes lie closely to within the mean average salt particle sizes used for the casting process. The mean openings between connecting pores decrease with increased casting pressure differentials and the pore volume fraction (porosity) predominantly

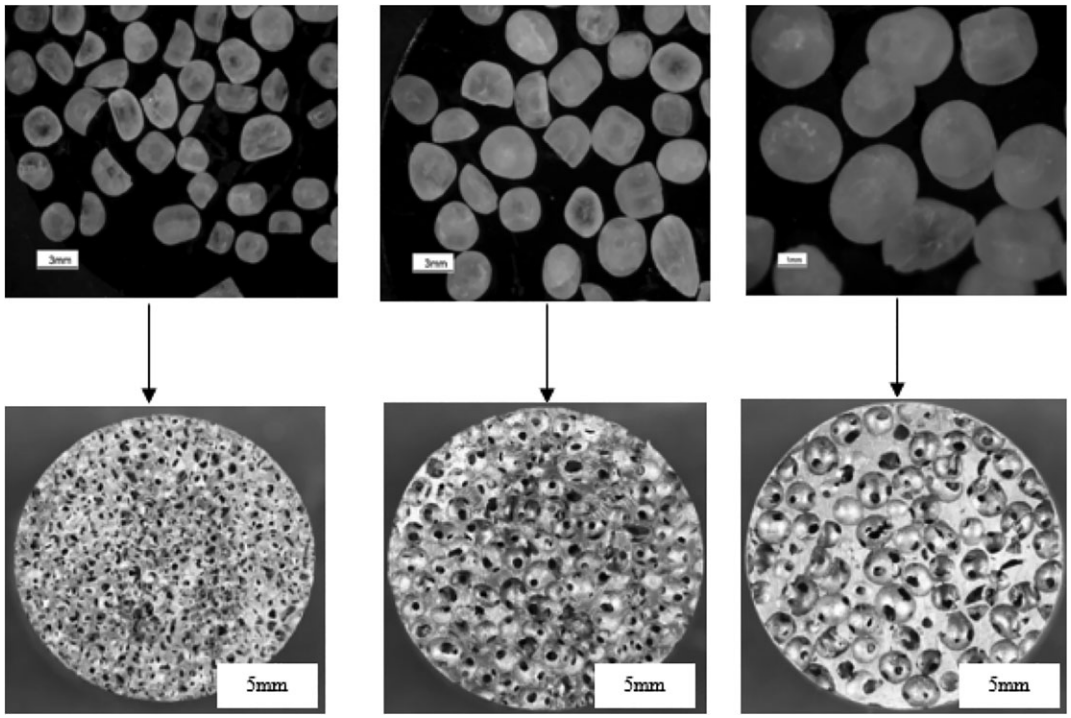

Figure 2. Top, scanning electron microscope (SEM) images of salts used for the casting process for particle size 1.0–1.4 mm/X1 (left), 2.0–2.5 mm/Y1 (middle), and 2.0–3.15 mm/Z1 (right), and bottom optical microscope images of foam structures produced with particle sizes 1.0–1.4 mm/X (left), 2.0–2.5 mm/Y1 (middle), and 2.0–3.15 mm/Z produced at 0.9 bar.

controlled by the packing density of the beds. Though, this is also affected by the variation in liquid infiltration pressure with lower pressure differential leading to the less complete filling of the interstices of the packed beds and the higher level of porosity as shown in Y4 structure.

Figure 2 confirms the shapes and sizes of the salt beads to dictate the morphology (Figure 3) and pore sizes of the structures, respectively. These also show smaller and multiple rounded "windows" or connectivity between near-spherical connecting pores and the size of these windows increases with increased pore/particle sizes and infiltration pressure differential used as presented in Table 1. Optical, SEM assessment, and tomography imaging of these structures reveal that not only the "window" sizes of the structures are affected with variation in pressure differentials but also the number of contacts (coordination number) between connecting pores is also affected. Previous work in Ref. 20,21 has shown that coordination number per cell is dependent on that obtained for packing of salt beds affected by variation in packing density and particle shapes and sizes. For monosized "virtual" near-spherical monosized structures of roundness close to unity, typical values between 6 and 7 are attained in Ref. 20,23 and higher for distorted near-spherical shaped salt beads in Ref. 22 used herein.

The experimental setup in Figure 4 was designed to accurately measure pressure drops across an open-celled aluminum foam structure at a defined flow rate of air movement. The experimental setup and measurement methods were designed like those reported in Ref. 14,15 and in brief, in Ref. 22. In detail, it consists of compressed air supply unit, a Norgren F74G 40um G ½ in. automatic pneumatic filter (working pressure 0/10 bar), a nickel-plated brass hydraulic needle valve series (FT 1251/2 & connection thread BSP 3/8 in.), standard (stable, easy-to-read, ±3% of full scale) precision-machined acrylic Flo-Rite™ air flow meters (0–140 LPM) a flow straightener, a mid-flange assembly of foam sample holder with a GEMS sensors pressure transducer (0–2.5/25 bar) and a data-log PC installed with 2016 NI LabVIEW signal for data acquisition.

A precisely machined foam sample of diameter 25 ± 0.2 mm, and foam thickness 34.5 ± 0.3 mm (conferred to be the maximum length of the sample holder in the mid-assembly without the need of a spacer) was wrapped with a polytetrafluoroethylene (PTFE) tape to prevent air-bypass by ensuring total control of air passage only through the pores and "windows" of the foam structure and as well maintain a tighter fit and greater coefficient of friction with the wall of the mid-flange typically, 21.183 mm internal diameter (flow diameter). The filter regulator made up of element material sintered polypropylene was used to remove water vapor and impurities (filtration size, 40 μm) from the air supply. Two pressure transducers were connected to both the inlet (0–2.5 bars) and outlet (0–25 bars) of the mid-assembly. Pressure–transducer voltage calibration was done using a digital pressure indicator (DPI 601) for the inlet transducer (0–2.5 bars) while the outlet pressure was conferred to be atmospheric.

An unmitigated power supply was ensured by using 3 × 9 V nonrechargeable batteries supplying 8–30 V GEM transducers. This was done to minimize noise effects and as well minimize the gap in error band. The needle valve with a minimum and maximum operating temperature of −20 to +100 °C and 210 bars maximum operating pressure was used to control the outflow of air into the flow meter from the filter regulator operating at 2.5 bars. This nickel-plated brass hydraulic needle valve consists of a double-acting valve for controlling and shutting off the flow and a single-action valve for flow control with free counter-current. A plot of pressure and voltage difference measured across the foam structure shows a perfectly fitted (P–ΔV) linear correlation (Figure 5) of mean standard deviation 1.63 and 0.77% determined for the

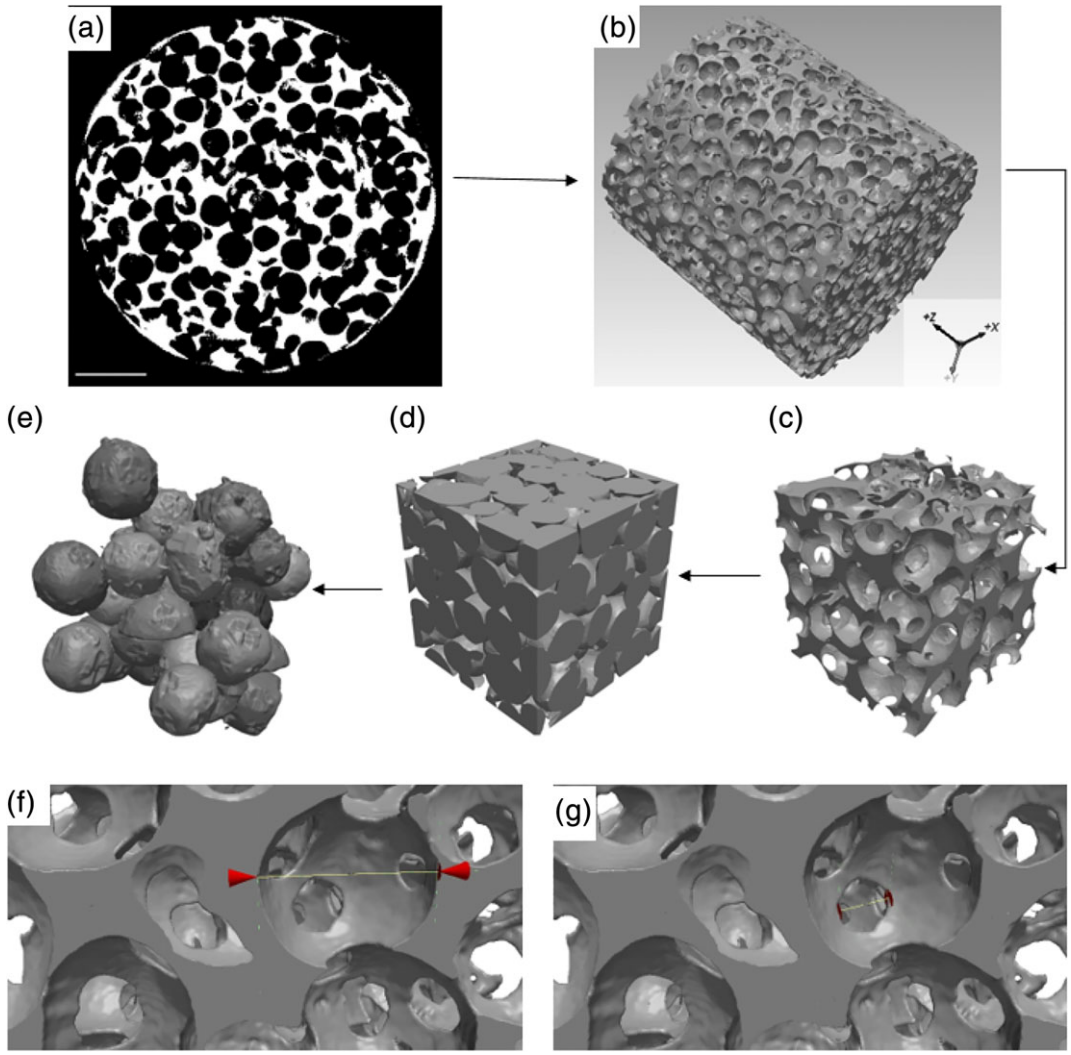

Figure 3. (a) Two-dimensional computerized tomography image, (b) three-dimensional reconstructed, (c) representative structural phase, (d) representative fluid phase, (e) segmented pores, (f) typical pore sizes measurement, and (g) pore openings of measurement of Y1 "bottleneck" structure.

[Color figure can be viewed at wileyonlinelibrary.com]

inlet and exit transducers, respectively. A minimum steady time of 2 min was allowed before taking the average sum of 2000–3000 V data recorded in a space of 2–3 min by the data acquisition PC device translating to upstream and downstream gauge pressures.

The flow meter available in metric scales was used to determine the air flow rate (0–140 LPM) before it flows through the mid-flange (sample holder) via the flow straightener. Upstream and downstream air pressures drop across the foam sample were taken with the help of the GEMS pressure transducers and data-log for the given range of flow rates. The measured upstream and downstream gauge pressures were converted to absolute pressures by simply adding the measured gauge pressures with atmospheric pressure.[9,14,24,25] Due to the fractional change in the air as opposed to liquid, care was taken to account for compressibility effects to avoid significant underestimation of the static pressure variation caused by an alteration in the density of the flowing fluid (air) across the foam cross section.[9,15,26,27] Equation 5 was applied to determine the "real" pressure drop (ΔP) across the structure as a function of the inlet (P_i) and outlet (P_0) absolute

Table 1. Measured Structural and Flow Parameters of the Porous Al Structure

Sample	Infiltration Pressure Difference, Pi (bar)	Porosity, Ø (%)	Mean Pore Size, Dp (mm)	Mean Connectivity, Dw (μm)	Permeability, $k_0/10^{-09}$ (m^2)	Forchheimer Coefficient, C_F [−]
EXPT-X1	0.90	72.03	1.21 ± 0.18	275 ± 10	4.16	0.92
EXPT-Y1	0.90	70.55	2.21 ± 0.15	643 ± 17	13.37	2.03
EXPT-Y2	0.60	72.55	2.23 ± 0.12	728 ± 24	17.00	0.71
EXPT-Y3	0.45	75.09	2.22 ± 0.16	727 ± 15	19.26	0.62
EXPT-Y4	0.25	78.22	2.25 ± 0.24	920 ± 25	31.24	0.29
EXPT-Z1	0.90	75.08	2.75 ± 0.21	710 ± 23	18.98	0.89

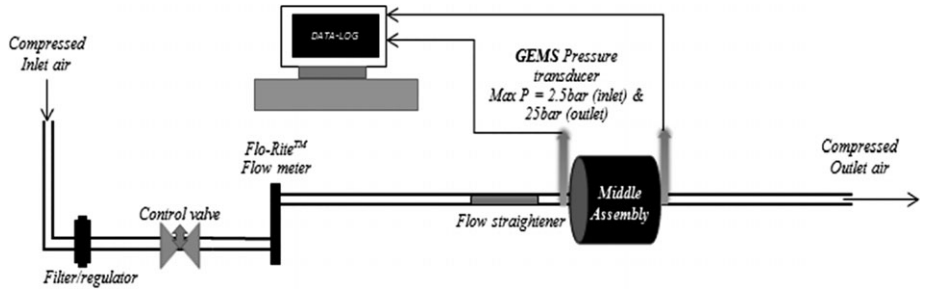

Figure 4. Schematic representation rig set up to measure air flowing across porous metallic structures.
Adapted from Ref. 22.

pressures while P_R was taken as reference or atmospheric pressure.

$$\Delta P = \frac{P_i^2 - P_o^2}{2P_R} \tag{5}$$

To ensure that accuracy of the experimental setup in Figure 4 is preserved and the right data were obtained, care was taken to the first test for leak detection and an airflow measurement on a 20 mm thick Inconel 450 μm (metal alloy) foam sample (Figure 6) of density and pore volume fraction, 828 kg m^{-3} and 84%, respectively was carried out and compared to existing data available in the literature.[15] A plot of pressure drops per unit length (Pa m^{-1}) against superficial air inlet velocity (m s^{-1}) for the Inconel foam structure followed a second-order Forchheimer relation (Eq. 1) and a reasonable agreement of 99.7% was attained in comparison with the literature data.

Also, airflow measurement through a 12 mm thick Recemat RCM-NCX 1723 sample shows reasonable agreement with numerically simulated (using x-ray tomography images of the "real" structure) and measured values of unit pressure drop developed across the foam sample reported in Ref. 28. Though, flow length reported in Ref. 28 was said to have a considerable influence on the flow performance due to the inhomogeneous topology (combination of irregular dodecahedron and tetrakaidecahedron cell with pentagonal faces described in Ref. 29) of the sample geometry resulting in a nonuniform connectivity and variable length thereby necessitating a more developed flow field (increased computational time) to fully describe the entire flow behavior in a large sample especially at higher flow velocities. Flow behavior through porous aluminum structures herein may differ from the Inconel 450 μm and Recemat RCM-NCX 1723 samples but the observable agreements between the measured and literature data confirm the precise experimental setup and the sureness of any measured data of unit pressure drop across structures of any morphology, cell sizes, and openings.

Experimental,[5,9,18,25,30] analytical,[17] and computational models[21,31-35] available in the literature have shown that the pressure drop developed across a porous body presented to a flowing fluid, is a function of its thickness and the superficial inlet fluid velocity. The unidirectional, steady state, and fully developed pressure drop of airflow across Z1 (2.5–3.15 mm) aluminum foam structure was measured repeatedly (reassembling the experimental setup and flipping both sides of the foam structure) at different air superficial velocity typically between 0.6 and 6.63 m s^{-1} (14–140 LPM) and was divided by its porous body thickness (L = 34.5 mm) to determine the pressure drop per unit length ($\Delta P/L$) presented in Figure 7. Also, a reduced pressure drops ($\Delta P/LV$) was determined by diving the pressure drop per unit length against superficial air inlet velocity presented in Figure 8.

For the range of fluid velocity (0.6–6.63 m s^{-1}) studied, the relationship between the developed pressure drop gradient across the porous structure (Z1) and superficial fluid velocity can simply be described by the third-term cubic Forchheimer relation (Eq. 4) to extract the viscous and inertial terms. Figure 8 shows a clear distinction between the range of fluid velocity which clearly follows second- and third-order Forchheimer relation. This shows that fluid velocity ranging between 0.6 and 2.36 m s^{-1} (14–50 LPM) obeys the second-order Forchheimer relation with a correlation of 99.33%. Hence, the viscous (permeability) and

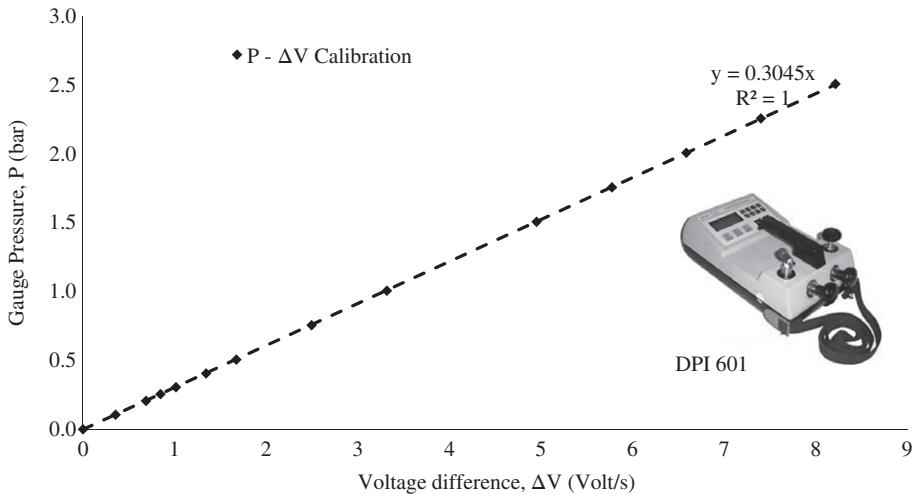

Figure 5. Inlet pressure–voltage calibration a digital pressure indicator (DPI 601).

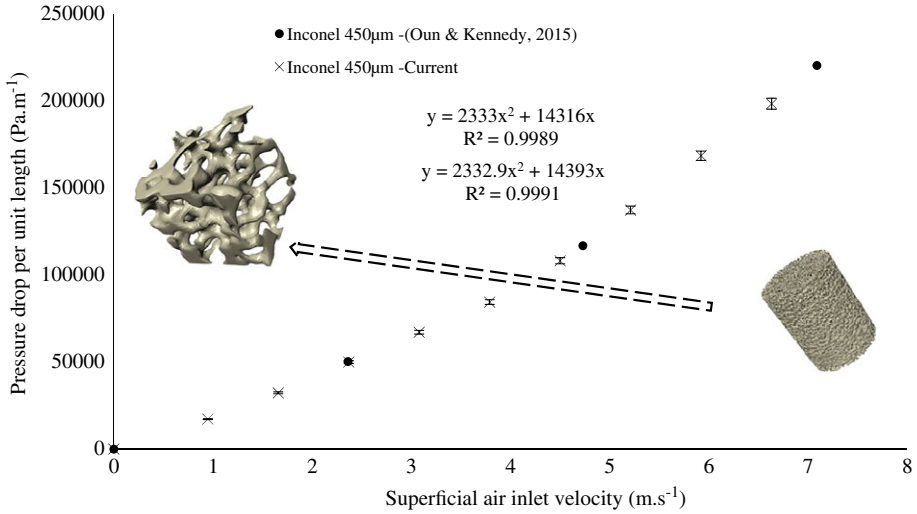

Figure 6. X-ray CT images of Inconel 450 µm foam structure and a plot of pressure drops per unit length (Pa m^{-1}) against superficial air inlet velocity (m s^{-1}) for the structure.

[Color figure can be viewed at wileyonlinelibrary.com]

inertial (form drag) terms of this fluid flow behavior can easily be determined using the second-order quadratic model of Hazen–Dupuit–Darcy (Eq. 1) fit of a pressure gradient to superficial velocity. Above this velocity range, a third-order Forchheimer relation is observed for a correlation of 99.43%. A detailed understanding of the flow behavior and the regime of occurrence is done using Darcy–Weisbach approach.

Reynolds Number and Friction Factor Relation

In practically all cases, the term Darcy's law for flow through porous structures is valid providing its mean pore/particle diameter-based Reynolds number (Re_D) does not exceed some value between 1 and 10.[18] Lage et al[36] specified this regime to be a transition from Darcy to Forchheimer while complete Darcy regime was reported to exist at $0 \le Re_D \le 1.0$. Similarly, complete laminar, laminar-turbulent transition, and fully developed turbulent regimes were reported for Reynolds number between 10–150, 150–300, and >300, respectively. A more simplified approach to understanding the pattern of flow and regime of manifestation is the use of Darcy–Weisbach approach usually done by plotting a dimensionless Fanning friction factor (f_F) against mean pore diameter-based Reynolds number[18,21] as shown in Figure 9 for Z1 structure, typically with the largest cell sizes and highest differential pressure. Optical images of this structure revealed a mean pore size of 2.77 mm measured and was taken as the characteristic linear dimension (D_P) of the "bottleneck-type" structure as used in Ref. 29. Mathematical representations of the Fanning friction factor (f_F) and pore diameter-based Reynolds number (Re_D) are presented in Eqs. 6 and 7 as a function of pressure drop (ΔP), superficial velocity (V), mean pore diameter or characteristic linear dimension (Dp), fluid density (ρ), and fluid dynamic viscosity (μ).

$$f_F = \frac{\Delta P}{\left(\rho V^2/2\right)} \tag{6}$$

$$Re_D = \frac{\rho V D_P}{\mu} \tag{7}$$

Notable observations from the plot are the range of values estimated for the Reynolds number, typically to within 122–1221 for

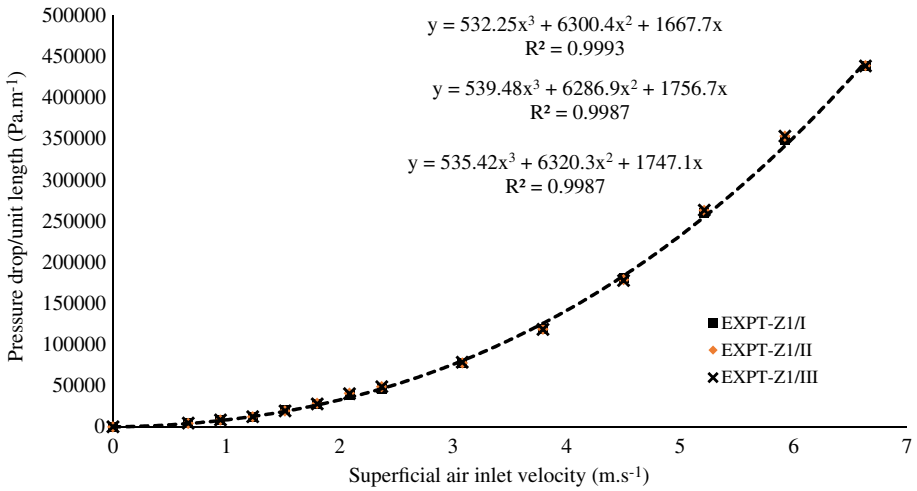

Figure 7. Experimental pressure drops per unit length (Pa m^{-1}) against air superficial inlet velocity (m s^{-1}) for a repetitive test on aluminum foam sample Z1 (2.5–3.15 mm).

[Color figure can be viewed at wileyonlinelibrary.com]

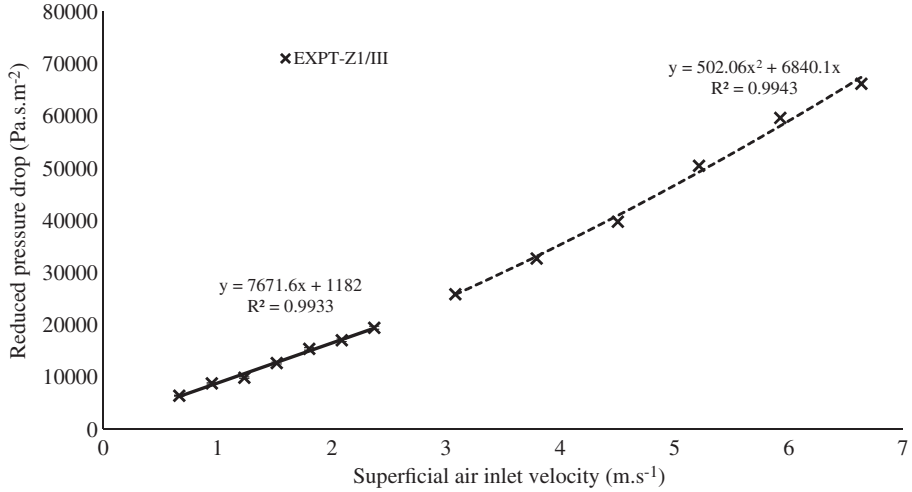

Figure 8. Experimentally reduced pressure drops (Pa.s m^{-2}) against air superficial inlet velocity (m s^{-1}) for a repetitive test on aluminum foam sample Z1 (2.5–3.15 mm).

the specified velocity range (0.6–6.6 m s^{-1}) and the regimes of manifestation with increased fluid velocity in the porous structure. Below 435 value of Reynolds number ($v_s \leq 2.36$ m s^{-1}), there exists a power law relationship between the Fanning friction factor and Reynolds number. Viscous forces predominate inertial forces at the lower end of this laminar flow regime while inertial forces predominate viscous forces at the upper end of this regime. This regime is termed as the nonlinear laminar flow regime and can be simply be described by the second-order Forchheimer relation (Eq. 1). The permeability (k_0), Form drag (C), and Forchheimer coefficient (C_F) determined in this regime are 18.98×10^{-09} m^2, 6474.63 m^{-1}, and 0.89, respectively.

A significant contribution of wall function (increased Form drag) deviates its behavior away from power law and this regime is termed as the transition regime. In this case, the transition from laminar to turbulent flow exists for velocity and Reynolds number range of $2.36 \leq v_s \leq 2.72$ m s^{-1} and $435 \leq Re_D \leq 494$, respectively. As Re_D increases beyond 494, the turbulent flow is observed (Darcy's law not valid) and inertial forces completely dominate the fluid flow across the porous structure. This is an indication that high flow velocity of the fluid through a porous media is a major contributory factor in attaining turbulence[36] while the nonlinearity deviation from Darcy is caused by inertial effects[9,37] and not turbulence although the flow is laminar for $Re_D \leq 435$.

Other foam structures conformed to having a similar trend of the Darcy–Weisbach approach, but their Reynolds number and friction factor differ from each other due to the variation in the structural parameters resulting from the use porogens of different sizes and the important applied differential pressure used during the casting process. A typical example of this is the flow behavior through foam structure X1 made with packed porogens with the least particle sizes in the range of 1.0–1.4 mm and at 0.9 bar liquid foam infiltration pressure. Darcy–Forchheimer, transition regime and turbulent regime for flow through this structure were attained for pore diameter-based Reynolds number, typically in the range of $48 \leq Re_D \leq 152$, $152 \leq Re_D \leq 173$, and $173 \leq Re_D \leq 485$, respectively (Figure 10). Similarly, the ranges of Reynolds numbers attained for these regimes for flow through the Y4 structure with the largest openings are $97 \leq Re_D \leq 453$, $453 \leq Re_D \leq 663$, and $663 \leq Re_D \leq 977$ presented in Figure 11.

Understanding this flow pattern is necessary toward the determination of viscous (permeability) and inertial (Form drag and Forchheimer coefficients) of fluid flow through porous structures of any topology and cell sizes. Though, the square root of permeability ($\sqrt{k_0}$) has been reported in the literature[38-40] to be

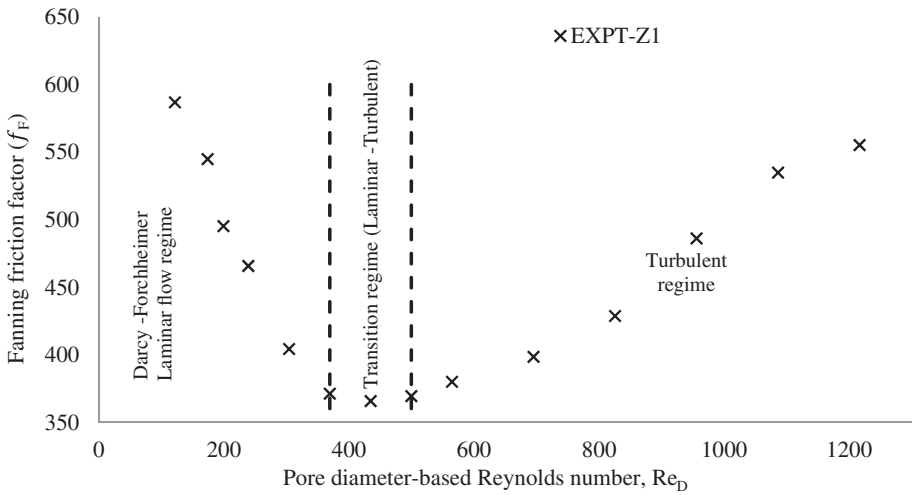

Figure 9. Plots of dimensionless Fanning friction factor (f) against pore diameter-based Reynolds number (Re_D) for airflow through the lowest window-sized (Z1) porous Al foam structure.

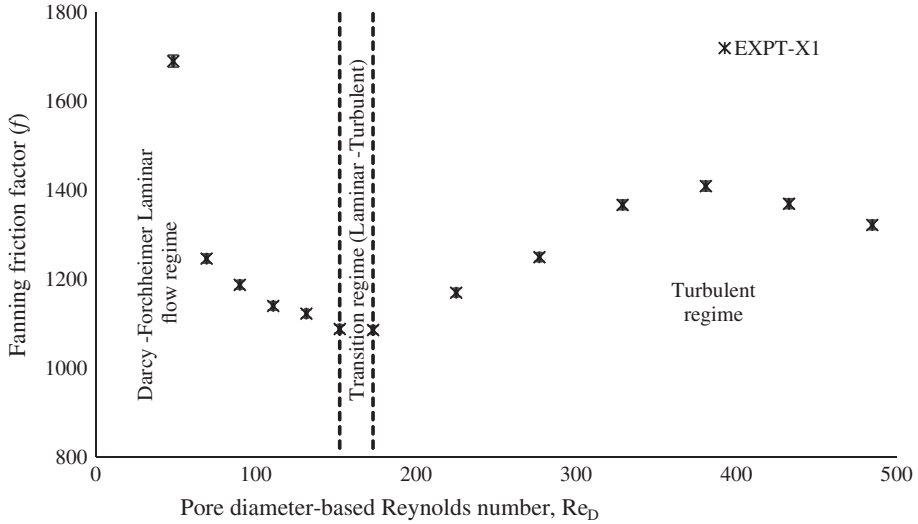

Figure 10. Plots of dimensionless Fanning friction factor (f_F) against pore diameter-based Reynolds number (Re_D) for airflow through the lowest window-sized (X1) porous Al foam structure.

useful in defining the true characteristic linear dimension of the structure due to fact that the permeability and not cell size represents more the inherent morphology of the porous structure. A plot of the Fanning friction factor against the permeability-based Reynolds number may indicate low values of Reynolds number but the behavioral trends from Laminar to Turbulent regime remain the same irrespective of the choice of characteristic linear dimension chosen.

Pressure Drop Data

A plot of the unit pressure drop (Pa m^{-1}) measured for the six porous structures for the different range of pore sizes and differential pressures against the superficial air inlet velocity (m s^{-1}) is presented in Figure 12. This polynomial trend can be fully described by the second-order Darcy–Dupuit–Forchheimer model with flow regime particularly to be within Laminar using Figures 7–11. Dividing the pressure drop per unit structural thickness measured for all the six foam samples by the superficial velocity (reduced pressure drop) and plotting against the superficial air inlet velocity as reported in Refs. 9,16, the laminar flow unit pressure drop (Figure 12) can be further substantiated and to ensure the accurate values of the viscous and inertial terms are obtained. Such a plot is presented in Figure 13 for all the structures with a linear dependence fit ($R^2 > 99\%$) indicating the measured pressure drops to be within the Forchheimer regime except for the X1 structure with the lowest cell sizes. Flow through this X1 structure indicates the presence of Darcy regime for the first two velocities with little or insignificant difference between their reduced pressure drops and Forchheimer regime exist for flow between 0.9 and 2.36 m s^{-1} with a linear dependence of very close fit.

The difference and order of magnitude in the measured unit pressure drop for all the foam structures can be classified into low-, mid-, and high-pressure drop. Higher values of pressure drops are observed for samples with the lowest porosities (X1 and Y1) while the lowest pressure drop is attained for the sample (Y4) with largest openings and conferred to have the highest porosity value (Table 1). The similarity in the intermediate pressure drop attained for the Y2, Y3, and Z1 structure

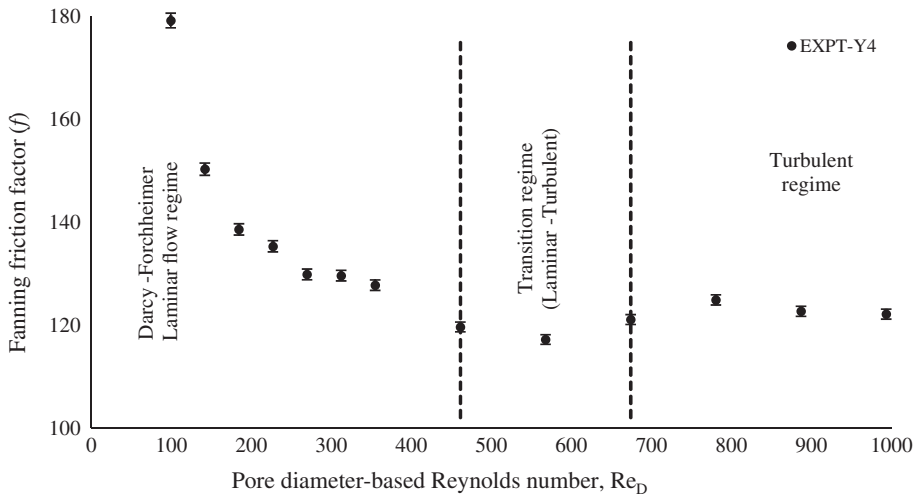

Figure 11. Plots of dimensionless Fanning friction factor (f_F) against pore diameter-based Reynolds number (Re_D) for airflow through the largest window-sized (Y4) porous Al foam structure.

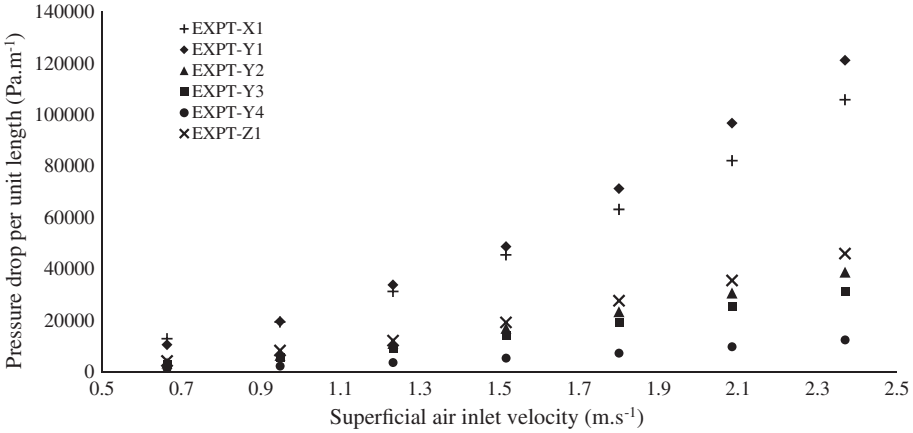

Figure 12. Plots of measured pressure drop per unit length (Pa m^{-1}) against superficial air inlet velocity (m s^{-1}) six foam structures.

is greatly influenced by the minimal difference in the changes associated with porosity and openings between the connecting cell sizes within the microstructures.

The size of the pores within the porous structure influences the tortuous path (tortuosity) and interstices available as pore volume for the flow of fluid (air). Larger pore sizes (opposed to smaller pore sizes) yielded a low tortuous path (tortuosity), low specific surface and large fluid volume which invariably resulted in low-pressure drops and high permeability of fluid measured across the foam structures. This flow trend is observed for foam X1, Y1, and Z1 structures (produced using similar liquid pressure differential of 0.9 bar) at very low velocity were the flow behavior of the structure are largely dependent on the openings of the structures.[38] At high velocity greater than 1 m s^{-1}, the high pressure drops attained for Y1 structure when compared to the X1 structure are largely due to thickened ligaments resulting in the low porosity value of the Y1 structure and thereby providing more resistance to the flowing fluid across the structure. Optical imaging of these structures (Figure 1) revealed a near-spherical structure for the Y1 structure while the X1 structure consists of highly irregular-shaped, inhomogeneous cells and large "window" to pore ratio (resulting from more half sized spherical salts used during casting), thereby providing lesser resistance to flowing fluid at high velocities.

The behavior of airflow through this structure is also affected by the number of "windows" (coordination number) existing with the porous matrix, typically, flow through Y structures made for different liquid differential pressures. At high infiltration pressures, liquid foams (aluminum) are forced into spaces created by packed beds of porogens thereby reducing the size and the number of "windows" available for permeation of fluid. Reported in Ref. 22, for samples having similar pore sizes and differential pressures, a plot of the ratio of "window" to pore size against the liquid pressure differential indicates a power inverse relation between these parameters. It is evident from this Table 1 that at low differential pressure, the connectivity (openings) between connecting pores within the porous structure is larger than that produced at high infiltration pressure provided the similar pore sizes are maintained. Lower pressure drops per unit foam thickness and the largest "window" sizes are associated with the lowest infiltrated pressure Y1 sample (high capillary interaction between connecting pores) while a reverse order of macroscopic and flow data was obtained for the highest liquid infiltrated pressure Y1 structure (low capillary interaction between connecting pores). Tabular representation detailing values of the structural and flow

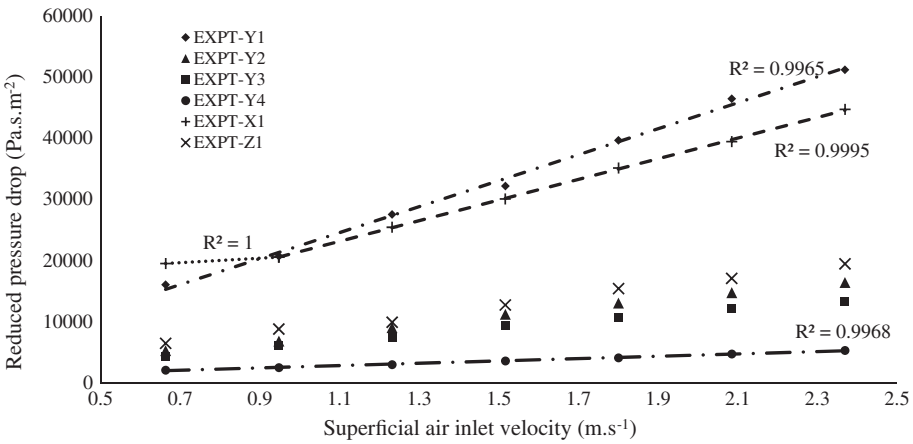

Figure 13. Plots of reduced pressure drop per unit length (Pa m^{-1}) against superficial air inlet velocity (m s^{-1}) six foam structures.

parameters of the all the six porous structures studied herein are presented in Table 1.

Conclusion

Structural characterization and measurements of airflow across porous metallic structures typically, of the bottleneck-type thereof, have been presented. The permeability of the structures is said to greatly depend on the sizes of the "bottleneck" between connecting pores, typically, higher for larger apertures and lower for smaller apertures. The inertial term increases for the low-density structures and decreases for high-density structures having wider openings. Lower pore sizes were reported to give low permeability with greater resistance to flowing fluid, else, for the larger pore size structures. CFD modeling and simulation of laminar airflow across "virtually-created" structures imitating the fluid-structural domain of this "real" structures and an extension to bimodal structures could be considered to ease rapid understanding of flow behavior of this material at low operating cost and flexibility resulting from changes of pore diameter sizes and openings.

Acknowledgments

OAJ would like to thank the University of Nottingham, Bowers and Wilkins Group, Simpleware—Synopsys Technology and Petroleum Technology Development Fund for providing the funds, licenses, technical support needed for the completion of this work.

Literature Cited

1. Zimmerson RW. *Equation for Fluid Flow in Porous Rocks*. London, UK: Department of Earth Science and Engineering, Imperial College; 2003.
2. Heijs AWJ, Lowe CP. Numerical evaluation of the permeability and Kozeny constant for two types of porous media. *Phys Rev E Stat Phys Plasmas Fluids Relat Interdiscip Topics*. 1995;51:4346-4352.
3. Dias R, Teixeira JA, Mota M, Yelshin A. Tortuosity variation in a low-density binary particulate beds. *Sep Purif Technol*. 2006;51(2):180-184.
4. Karimian SAM, Straatman AG. CFD study of the hydraulic and thermal behaviour of spherical-void-phase porous materials. *Int J Heat Fluid Flow*. 2008;29:292-305.
5. Liu HL, Hwan HR. Permeability prediction of fibrous porous media with complex 3D architectures. *Composite Part A*. 2012;43:2030-2038.
6. Ozgumus T, Mobedi M, Ozkol U. Determination of Kozeny-constant based on porosity and throat size ratio in porous medium with rectangular rods. *Eng Appl Comput Fluid Dyn*. 2014;8(2).
7. Zhou J. *Porous Metallic Materials. Advanced Structural Materials*. Vol 22. Taylor & Francis Group; 2006.
8. Habisreuther P, Djordjevic N, Zarzalis N. Statistical distribution of residence time and tortuosity of flow through open-celled foams. *J Chem Eng Sci*. 2009;64:4943-4954.
9. Dukhan N. *Metal Foams: Fundamental and Applications*. Pennsylvania: DESTECH Publication, Inc. Technology & Engineering; 2013:1-310.
10. Dukhan N, Bagci O, Ozdemir M. Experimental flow in various porous media and reconciliation of Forchheimer and Ergun relation. *Exp Thermal Fluid Sci*. 2014;57:425-433.
11. Ranut P, Nobile E, Mancini L. High-resolution microtomography-based CFD simulation of flow and heat transfer in aluminium metal foams. *J Appl Thermal Eng*. 2013;11:56.
12. Innocentini DMM, Salvini VR, Macebo A, Pandolfelli VC. Prediction of ceramic foams permeability using Ergun equation. *Mater Res*. 1999; 2:283-289.
13. Tadrist L, Miscevis M, Rahli O, Topin F. About the use of fibrous materials in compact heat exchangers. *Exp Thermal Fluid Sci*. 2004;28:193-199.
14. Oun H, Kennedy AR. Experimental investigation of pressure drop characterization across multilayer porous metal structure. *J Porous Mater*. 2014;21:1133-1141.
15. Oun H, Kennedy AR. Tailoring the pressure drop in multi-layered open-cell porous inconel structures. *J Porous Mater*. 2015;2:1627-1633.
16. Harker JH, Richardson JF, Backhurst JR. *Chemical Engineering*. Vol 2. 5th ed. Oxford: Butterworth-Heinemann; 2002:193-233.
17. Du Plessis JP, Wouldberg S. Pore-scale derivation of Ergun equation to enhance its adaptability & generalization. *Chem Eng Sci*. 2008;63: 2576-2586.
18. Bear J. *Dynamics of Fluids in Porous Media*. New York: Dover Publications, Inc; 1972:124-130.
19. Kennedy AR. Porous metals and metal foams made from powders. In: Kondoh K, ed. *Powder Metallurgy*. InTech; 2012. ISBN:978-953-51-0071-3.
20. Langston P, Kennedy AR. Discrete element modelling of the packing of spheres and its application to the structure of porous metals made by infiltration of packed beds of NaCl beads. *Powder Technol*. 2014;268:210-218.
21. Otaru AJ, Kennedy AR. The permeability of virtual macroporous structures generated by sphere packing models: comparison with analytical models. *Scr Mater*. 2016;124:30-33.
22. Otaru AJ, Morvan HP, Kennedy AR. Measurement and simulation of pressure drop across replicated microcellular aluminium in the Darcy-Forchheimer regime. *Acta Mater*. 2018;149:265-273.
23. Asmar BN, Langston PA, Matchett AJ. A generalized mixing index in discrete element method simulation of vibrated particulate beds. *Granular Matter*. 2002;4(3):129-138.
24. Khayargoli P, Loya V, Lefebvre LP, Medraj M. The impact of microstructure on the permeability of metal foams. *CSME Forum*. 2004; 220-228.
25. Mostafid AM. *Entrance and Exit Effect of Flow through Metallic Foams*. Quebec, Canada: Department of Mechanical & Industrial Engineering, Concordia University; 2007.
26. Bonnet JP, Topin F, Tadrist L. Flow laws in metal foams: compressibility and pore size effects. *Trans Porous Med*. 2008;73:149-163.
27. Edouard D, Lacroix M, Huu CP, Luck F. Pressure drop modelling on solid foam: state-of-the-art correlation. *Chem Eng J*. 2008;144:299-311.
28. De Carvalho TP, Morvan HP, Hargreaves D, Oun H, Kennedy A. Pore-scale numerical investigation of pressure drop behaviour across open-cell metal foams. *Tran Porous Med*. 2017;117(2):311-336.
29. Weaire D, Phelan R. A counter-example to Kelvin's conjecture on minimal surfaces. *Philos Mag Lett*. 1994;69:107-110.
30. Antohe B, Lage JL, Price DC, Weber RM. Experimental determination of the permeability & inertial coefficients of mechanically compressed aluminium metal layers. *ASME J Fluids Eng*. 1997;11:404-412.
31. Peng S, Hu Q, Dultz S, Zhang M. Using X-ray computed tomography pore structure characterization for Berea sandstone: resolution effect. *J Hydrol*. 2012;472–473:254-261.
32. Petrasch J, Wyss P, Steinfeld A. Tomography-based Monte Carlo determination of radiative properties of reticulated porous ceramics. *J Quant Spectrosc Radiat Transf*. 2007;105:180-197.
33. De Carvalho TP, Morvan HP, Hargreaves D. Pore-Level Numerical Simulation of Open-cell Metal Foams with Application to Aero Engine Separators. Turbine Technical Conference and Exhibition, 2014; Dusseldorf, Germany.
34. Otaru AJ, Morvan HP, Kennedy AR. Modelling and optimisation of sound absorption in replicated microcellular metals. *Scr Mater*. 2018b; 150:152-155.
35. Otaru AJ. Enhancing the sound absorption performance of porous metals using tomography images. *Appl Acoust*. 2019;140:183-189.
36. Lage JL, Krueger PS, Narasimham A. Protocol for measuring permeability and form coefficient of porous media. *Phys Fluids*. 2005;17: 088101.
37. Boomsma K, Poulikakos D. The effect of comparison and pore size variations on the liquid flow characteristics in metal foams. ASME. *J Fluids Eng*. 2002;124:263-273.
38. Dybbs A, Edwards RV. A new look at porous media fluid mechanics-Darcy to turbulent. In: Bear J, Nato MY, eds. *ASI series E*; 1984.
39. Kececioglu I, Jiang Y. Flow through porous media of packed spheres saturated with water. *ASME J Fluids Eng*. 1994;116:164-170.
40. Kouidri A, Madani B, Roubi B. Experimental investigation of flow boiling in a narrow channel. *Int J Thermal Sci*. 2015;98:90-98.

Manuscript received Sep. 8, 2018, and revision received Nov. 12, 2018.